

# Biomimicking pit vipers' infrared sensing

Raffaele Di Giacomo<sup>1</sup>, Luca Bonanomi<sup>1</sup>, Vincenzo Costanza<sup>1</sup>, Bruno Maresca<sup>2</sup> and Chiara Daraio<sup>1</sup>

<sup>1</sup>Department of Mechanical and Process Engineering (D-MAVT), Swiss Federal Institute of Technology (ETH), Zurich, Switzerland.

<sup>2</sup>Department of Pharmacy, Division of Biomedicine, University of Salerno, Fisciano, Italy.

**Animals have evolved specialized tissues to sense temperature. Pit vipers have the most evolutionary advanced membrane that are used as infrared sensor to detect prey and predators at night. This membrane acquires its extraordinary sensitivity through voltage-gated ion channels of the wasabi heat receptor. So far, no engineered material with similar infrared sensitivity has been reported. Here we show that pectin films mimic the sensing mechanism and parallel the performance of the snakes' pit membrane. Pectin films react to distant infrared sources and can be used to map the temperature of surfaces. The films dramatically boost sensing capabilities and surpass the performance of existing synthetic skins. They can also be exploited in robotics to sense proximity of humans or animals.**

Snakes are cold-blooded animals and their body temperature corresponds to that of the environment. Snakes' pit membranes<sup>1</sup> (Fig. 1a, b) distinguish minute temperature variations. At night, mid-far infrared emission from a mammalian prey up to 1 m away cause small, local temperature increase on the membranes<sup>1</sup> (Fig. 1c). The small temperature increase leads to an increased opening of TRPA1 ion channels<sup>1-3</sup> and an increased current carried by Ca<sup>2+</sup> ions<sup>1</sup> (Fig. 1d) through the membrane. Interestingly, the mechanism of infrared detection<sup>4</sup> of the pit membrane is not photochemical since the radiated heat is not converted directly into electrical current<sup>1</sup>. Here we show that pectin-films (Fig. 1e) have temperature sensitivity comparable to the snake pit membrane.

Pectin, a component of all higher plant cell walls, is made of structurally and functionally very complex, acid-rich polysaccharides<sup>5</sup>. Pectin plays several roles in plants, for example, is an essential structural component of cell walls and binds ions and enzymes<sup>6</sup>. In high-ester pectins, at acidic pH, individual pectin chains are linked together by hydrogen bonds and hydrophobic interactions. In contrast, in low-ester pectins, ionic bridges are formed, at near neutral pH, between Ca<sup>2+</sup> ions and the ionized carboxyl groups of the galacturonic acid, forming an "egg box" in which ions are stored<sup>7</sup>. Pectin and pectates absorb in a wide band region of the infrared spectrum, ranging from far to near infrared<sup>8-11</sup>. Since the crosslinking between pectin molecules decreases exponentially with temperature<sup>12</sup>, increasing the temperature of a Ca<sup>2+</sup>-crosslinked pectin increases ionic conduction<sup>13</sup> (Fig. 1f). This can be exploited in temperature sensor with exquisite sensitivity.

We created a bulk hydrogel by adding CaCl<sub>2</sub> to a pectin solution (see Methods section). To test its thermal sensitivity, the gel was placed on top of two gold plated electrodes and dehydrated. After dehydration, the gel formed a film between the electrodes. We protected the samples from environmental humidity by soaking them in liquid polydimethylsiloxane (PDMS) (Supplementary Fig. S1a).

The pectin was dehydrated until the measured absolute water content was reduced to 30% in weight. Above this value, the conductivity of water is predominant and the measured total conductivity of the hydrogel is in the order of 28 mSm<sup>-1</sup> at room temperature. During

dehydration, the conductivity associated with water decreases, so that the conductivity of pectin becomes increasingly dominant. After dehydration, the conductivity of the hydrogel is in the order of  $0.1 \text{ mSm}^{-1}$ . Supplementary Figure S1b shows that the current-voltage characteristic of a typical film is linear.

To measure the response of the material in temperature, samples were heated on a plate, increasing the temperature from 8 to 39 °C (Supplementary Fig. S2). The thermal responsivity achieved was comparable with that of rat and rattle snakes' pit membranes (Fig. 1g). This value is comparable to the highest temperature responsivity on record<sup>13</sup>. The activation energy for our pectin film thermistor is 81.9 kJ/mol (Supplementary Fig. S2b and Supplementary Information), a value similar to that of the activation energy reported for pectin in rheological measurements<sup>12</sup>.

We also fabricated larger films (~200  $\mu\text{m}$  thick), by casting a pectin solution in a mold (see Methods). A thermal camera monitored the local temperature of the samples while an independent source meter measured their electrical current (Fig 2a). The films absorb infrared radiation (Fig. 2c) and respond with fidelity to intricate ambient temperature variations (Fig.s 2d and 2e). This also shows that upon heating and cooling the material experiences no hysteresis. The detailed data for a 2 sec time interval (Fig. 2e) reveal that the film senses small temperature variations with high signal to noise ratio.

The pit viper membrane sensitivity was estimated to be 1 mK or less, based on the snake's ability to detect preys at distance<sup>4</sup>. To compare the performance of our material to that of the viper's pit membrane, we characterized the sensitivity of pectin films to the presence of small, warm bodies at a distance. A microwavable teddy-bear was heated up to 37 °C. A thermal camera was used to determine its temperature and ensure it remained constant during the measurements. We placed the teddy-bear at 1 m distance from the membrane, for ca. 20 sec and then removed it. We repeated this procedure also for distances of 0.6 m and 0.4 m. The results show that the membrane in air detects warm bodies, about the size of a rat or a small rabbit, at up to 1 m (Fig. 2f), as hypothesized for the best performance of pit vipers<sup>1</sup>. From these measurements and the measurements in Fig. 2e, we estimate that the sensitivity of pectin films is 1 – 10 mK.

We also performed experiments with even larger films (21×29.7 cm) connected to two carbon electrodes (see Methods, Supplementary Video 1 and discussion). These samples have the same sensitivity as the one measured in small films (Fig. 1a). The ability to create large area sensors suggests the use of pectin films as synthetic skins.

Synthetic skins<sup>14</sup> are essential to augment robotics<sup>15</sup> and improve prosthetic limbs<sup>16</sup>. Existing platforms are designed to emulate properties of the human skin by incorporating artificial sensing functions<sup>16-20</sup>, such as response to temperature variations<sup>16,20-22</sup>. Synthetic skins that sense temperature variations use either passive, flexible resistors<sup>20-22</sup> or active electronic devices<sup>16</sup>. We compare the temperature responsivity (i.e., the signal variation in a given temperature increment) of pectin films with the best available synthetic skins<sup>16,20,22</sup>, in a biologically relevant, 30 K temperature interval (Fig. 3a). It is evident that the pectin films signal variation is at least one order of magnitude greater than the others<sup>16,20,22</sup>. A higher responsivity has only been reported in a very narrow temperature range (3-5 K) for a bistable device<sup>21</sup> (i.e., a temperature switch). However, synthetic skins require a larger range of operation to achieve a performance comparable to biological skins. The best reported sensitivity for synthetic skins has been estimated to be between 20-100 mK (Ref. 21). By comparison, pectin films reach a sensitivity of ~1 mK or less (see Fig. 2e).

Human skin senses temperature through ion channels<sup>3</sup> that belong to the family of the TRP sensors and include the snake TRPA1 orthologous<sup>3</sup>. Our pectin films mimic the TRP sensors, in that they also use Ca-ion regulation to mediate temperature sensitivity (Fig. 1). We fabricated skins (52 mm × 52 mm) with multiple electrodes (8 or 16 contacts) deposited on the external frame (Fig. 3). Skins were made of pectin films with chromium/gold electrical contacts sandwiched between two insulating layers (Fig. 3 b, c). The samples tested were supported by a rigid SiO<sub>2</sub> substrate and covered by a PDMS or acrylate layer (Fig. 3c). We monitored the signal between electrodes of each row and column while we increased the temperature in selected areas of the skins. Based on the number of contacts on the outer frame, we divided the area of the sample in four (or sixteen) blocks, corresponding to the number of “pixels”. Each pixel here is addressed as the intersection between each row and column, according to the electrodes’ position. This arrangement allowed us to reconstruct the temperature map on the material without cumbersome or pixel addressed electronics<sup>15,21</sup>. Mapping of complex temperature profiles can be further enhanced by algorithmic analysis of the temporal signal evolution.

The measurements obtained in the 4-pixel sample were performed using the circuit shown in Supplementary Fig. S4 and explained in the SI file. The position of a finger touching 4 different pixels of a skin for ~2 sec is clearly distinguishable from the electrical response of the materials (Fig. 3d). The voltage signals acquired are reported in Figs 3d, S5 and Tab. S1. The noise in Supplementary Fig. S5 derives from the electronic readout circuit and not from the sensor as confirmed performing similar measurements with a pico-amperometer (Supplementary Fig. S6). The temperature variation on each pixel was estimated to be less than 1 °C, as shown in the thermal image in Supplementary Fig. S7. To exclude piezo-resistive effects, we performed the same measurements touching the sample with a metal object at the same temperature of the pixel (Supplementary Fig. S8).

The temperature sensors in human skin are distributed with different spatial densities in distinct areas of the body<sup>23</sup>. To show the response of pectin skins to an increased sensing spatial density, we fabricated a 16-pixel device in the same skin area and tested its temperature mapping ability. We placed near the lower right corner of the skin an aluminum cube (12 mm × 12 mm × 3mm) at 26 °C (with ambient temperature of 20 °C). The signal map, measured on the skin 0.8 sec after the aluminum square was laid in contact, is shown in Fig. 3e for each of the 16 pixels (Supplementary Tab. S2). The thermal camera map (Supplementary Fig. S9 and pixelated in Fig. 3f) and the temperature map obtained with our skin show a very good match.

This work establishes that a material composed exclusively of purified plant pectin, engineered into a film, has a performance equivalent to that of the snake’s pit membrane and superior to other synthetic skins. The pectin films are ultra-low cost and scalable and can be used to boost temperature sensing in biomedical applications, and to augment the interactions of robots with humans.

## Material and Methods

To produce the materials, we used commercially available citrus low-methoxylated pectin (LMP) with a degree of methylation of 34% and a content of galacturonic acid of 84% (Herbstreith&Fox<sup>®</sup>). The pectin powder (2% w/vol) was dissolved at 80 °C in deionized water and stirred at 1,400 rpm until a uniform solution was obtained. To produce small films, a 32 mM CaCl<sub>2</sub> solution was added (corresponding to a stoichiometric ratio  $R = [Ca^{2+}]/2[COO^-] =$

1). The final gel, 0.47 mm × 0.47 mm × 2.75 mm in size, was deposited on contacts, 0.72 mm apart and dehydrated.

To obtain larger films, the pectin solution was poured into a Petri dish and a 32 mM CaCl<sub>2</sub> solution then added. After gelation, the highly hydrated films were transferred to a vacuum chamber and dehydrated at 12 mbar overnight. The final water content in the hydrogel was 30%. The samples were then detached from the Petri dish using a razor blade. The large samples shown in Supplementary Video 1 were produced on a glass substrate (28 cm × 30 cm × 0.5 cm) as the lower insulating layer. The electrical contacts were made of carbon tape, and a clear insulating acetate sheet (A4 paper format) was layered on top.

To produce the skins, the pectin solution was deposited directly on different substrates (PDMS or SiO<sub>2</sub>) with pre-deposited electrical contacts made by sputtering chromium/gold. In the experiments described in Fig. 1 and 2 a d.c. polarizing voltage of 20 V was applied to the samples and the current allowed to decrease for ca. 2 hours. After the initial discharge, the current remained stable for several hours (during which experiments were performed). We also performed a.c. measurements at different frequencies (see Fig. S10) on the same samples described in Fig. 1. We found no difference in the temperature response of the pectin films under a.c. or d.c. conditions (see Supplementary Information).

## References

1. E. O. Gracheva et al. Molecular basis of infrared detection by snakes. *Nature* **464**, 1006–1011 (2010).
2. Paulsen, C. E., Armache, J.-P., Gao, Y., Cheng, Y. & Julius D. Structure of the TRPA1 ion channel suggests regulatory mechanisms. *Nature* **525**, 511–517 (2015).
3. Vay, L., Gu, C. & McNaughton, P. A. The thermo-TRP ion channel properties and therapeutic implications. *British J. of Pharmacol.* **165**, 787–801 (2012).
4. Bakken, G. S. & Krochmal, A. R. The imaging properties and sensitivity of the facial pits of pitvipers as determined by optical and heat-transfer analysis. *J. Exp. Biol.* **210**, 2801 – 2810 (2007).
5. Sriamornsak, P. Chemistry of pectin and its pharmaceutical uses: A review. *Silpakorn Univ. Int. J.* **3**, 206–228 (2003).
6. Willats, W. G. T., McCartney, L., Mackie, W. & Knox, J. P. Pectin: cell biology and prospects for functional analysis. *Plant Mol. Biol.* **47**, 9–27 (2001).
7. Plazinski, W. Molecular basis of calcium binding by polyguluronate chains. Revising the egg-box model. *J. Comput. Chem.* **32**, 2988–95 (2011).
8. Synytsysya, A., Copikova, J., Matejka, P. & Machovic, V. Fourier transform Raman and infrared spectroscopy of pectins. *Carb. Pol.* **54**, 97–106 (2003).
9. Senè, C. F. B., McCann, M. C., Wilson, R. H. & Grinter, R. Fourier-Transform Raman and Fourier-Transform Infrared Spectroscopy. *Plant Physiol.* **106**, 1623–1631 (1994).
10. Kacurakova, M., Capek, P., Sasinkova, V., Wellner, N. & Ebringerová, A. FT-IR study of plant cell wall model compounds: pectic polysaccharides and hemicelluloses. *Carb. Pol.* **43**, 195–203 (2000).
11. Assifaoui, A., Loupiac, C., Chambin, O. & Cayot P. Structure of calcium and zinc pectinate films investigated by FTIR spectroscopy. *Carb. Res.* **345**, 929–933 (2010).
12. Cardoso, S. M., Coimbra, M. A. & Lopes da Silva, J. A. (2003) Temperature dependence of the formation and melting of pectin–Ca<sup>2+</sup> networks: A rheological study. *Food Hydrocoll.* **17**, 801–807 (2003).

13. Di Giacomo, R., Maresca, B. & Daraio, C. Plant nanobionics material with a giant temperature response mediated by pectin-Ca<sup>2+</sup>, *PNAS* **112**, 4541-4545 (2015).
14. Sun, J.-Y., Keplinger, C., Whitesides, G. M. & Suo, Z. Ionic skin. *Adv. Mater.* **26**, 7608-7614 (2014).
15. Kaltenbrunner, M. et al. An ultra-lightweight design for imperceptible plastic electronics. *Nature* **499**, 458–463 (2013).
16. Kim, J. et al. Stretchable silicon nanoribbon electronics for skin prosthesis. *Nature Commun.* **5**, 5747 (2014).
17. Tee, B. C.-K., Wang, C., Allen, R. & Bao, Z. An electrically and mechanically self-healing composite with pressure- and flexion-sensitive properties for electronic skin applications. *Nature Nanotech.* **7**, 825–832 (2012).
18. Nie, B., Li, R., Cao, J., Brandt, J. D. & Pan, T. Flexible transparent iontronic film for interfacial capacitive pressure sensing. *Adv. Mater.* doi:10.1002/adma.201502556
19. Tee, B. C. – K. et al. A skin-inspired organic digital mechanoreceptor. *Science* **350**, 313-316 (2015).
20. Segev-Bar, M., Landman, A., Nir-Shapira, M., Shuster, G. & Haick, H. Tunable touch sensor and combined sensing platform: toward nanoparticle-based electronic skin. *ACS Appl. Mater. Int.* **5**, 5531–5541 (2013).
21. Yokota, T. et al. Ultraflexible, large-area, physiological temperature sensors for multipoint measurements. *PNAS* doi: 10.1073/pnas.1515650112.
22. Park, J., Kim M., Lee Y., Lee, H. S. & Ko, H. Fingertip skin-inspired microstructured ferroelectric skins discriminate static/dynamic pressure and temperature stimuli. *Sci. Adv.* 2015;1:e1500661.
23. Nadel, E. R., Mitchell, J. W. & Stolwijk, J. A. J. Differential Thermal Sensitivity in the Human Skin. *Pflügers Arch.* **340**, 71-76 (Springer-Verlag 1973).

### **Acknowledgements**

The authors thank Ueli Marti (ETH Zürich, Institut für Mechanische Systeme) for the technical support in the realization of the electronic readout circuit and for useful discussions. This work was supported by the Swiss National Science Foundation, Grant #157162.

### **Author contributions**

R.D.G., L.B., V.C., B.M, and C.D. conceived the system and designed the research. R.D.G., L.B and V.C. designed and performed the experiments. R.D.G. and V.C. designed the readout circuit for the electrical measurements. All authors contributed to the analysis of the data and discussions. R.D.G., L.B. and V.C. prepared the figures. R.D.G, V.C., L.B. and C.D. designed the supplementary video. L.B. edited the video. R.D.G., B.M. and C.D. wrote the paper.

### **Additional information**

Supplementary information is available in the online version of the paper.

### **Competing financial interests**

The authors declare no competing financial interests.

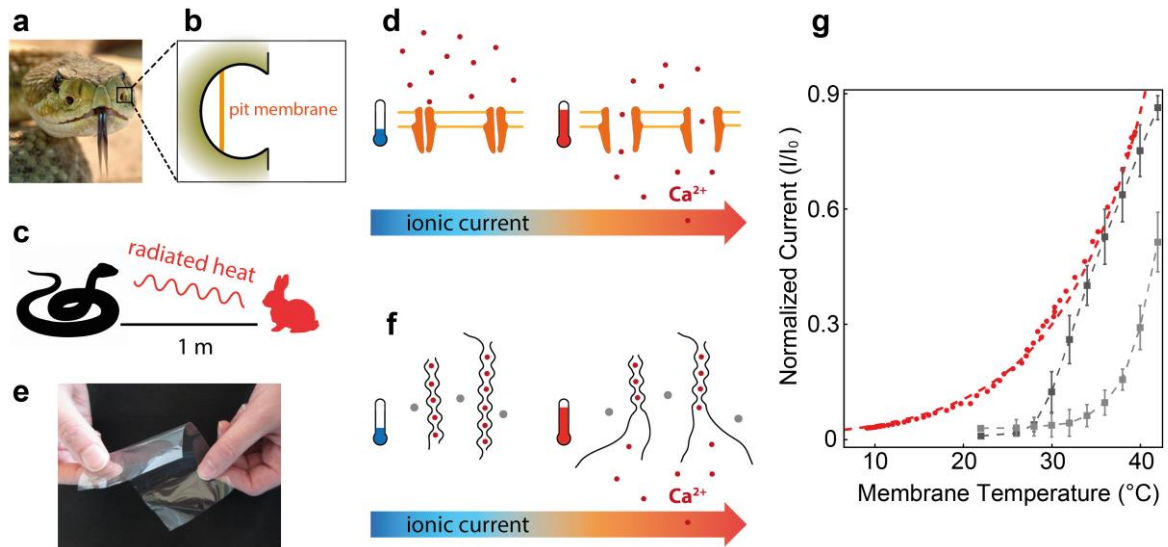


**Figure 1 | Comparison between pit membrane and pectin film.** **a**, Digital image of a rattle snake. **b**, Schematic of the pit organ and pit membrane. **c**, Schematic of the prey detection through infrared sensing. **d**, Molecular mechanism governing pit membrane sensitivity. Dark orange: TRPA1 channels. Light orange: cell membrane. Red dots: calcium ions. **e**, A sample of the produced pectin film. **f**, Molecular mechanism governing pectin film sensitivity. Black lines: galacturonic acid. Red dots: calcium ions. Grey dots: water molecules. **g**, Red dots: normalized current in a pectin film thermometer, the curve is obtained sampling current and temperature every 1 sec, up to 30  $^{\circ}\text{C}$ , and every 4 sec, up to 39  $^{\circ}\text{C}$ . Red dashed line: exponential fitting. The points with error bars and dotted lines are plotted from Gracheva *et al.* Dark grey dots: rattle snake. Light grey dots: rat snake.

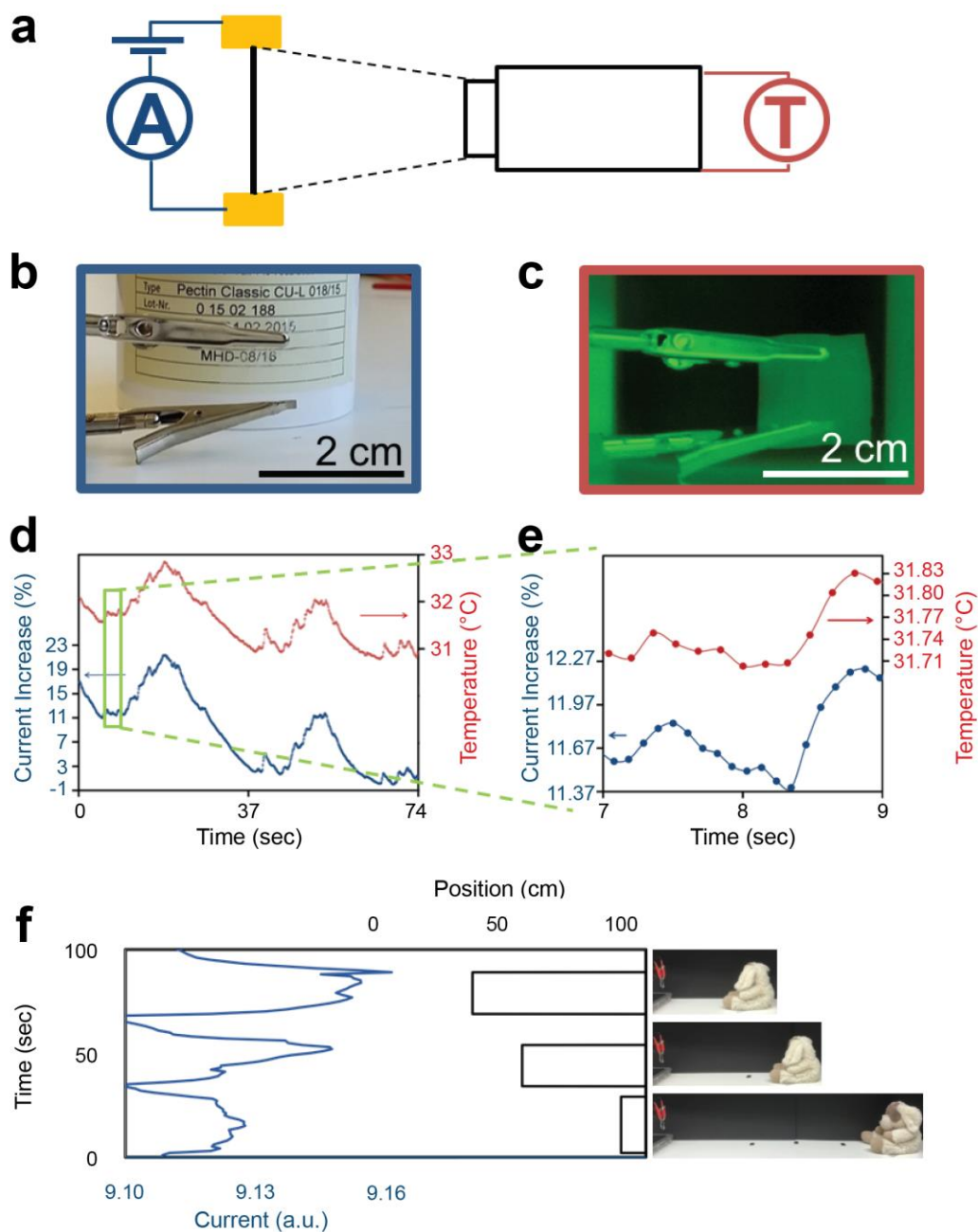


**Figure 2 | Characterization of the pectin film.** **a**, Schematic diagram of the measurement setup: a thermal camera acquires the temperature on the surface of a pectin film while two electrodes connected to a source meter measure its current at a constant applied voltage. **b**, Digital image of a transparent pectin film suspended between two electrodes (stainless steel clamps). **c**, Thermal-camera image of the pectin film shown in **(b)**. **d**, Experimental measurements of the electrical current in the pectin film (blue line, left axis) plotted as a function of time and compared to the sample's temperature measured by the thermal camera (red line, right axis). The temperature oscillations are caused by variations of the ambient temperature during the measurements. **e**, Magnification of the data in the green box in panel **d**. The solid dots represent measurement points and the lines are included as a guiding reference. **f**, Infrared sensing of a warm object (37 °C) at a distance. Blue line: current in the pectin film. Black line, position of the object with respect to the membrane positioned in 0.

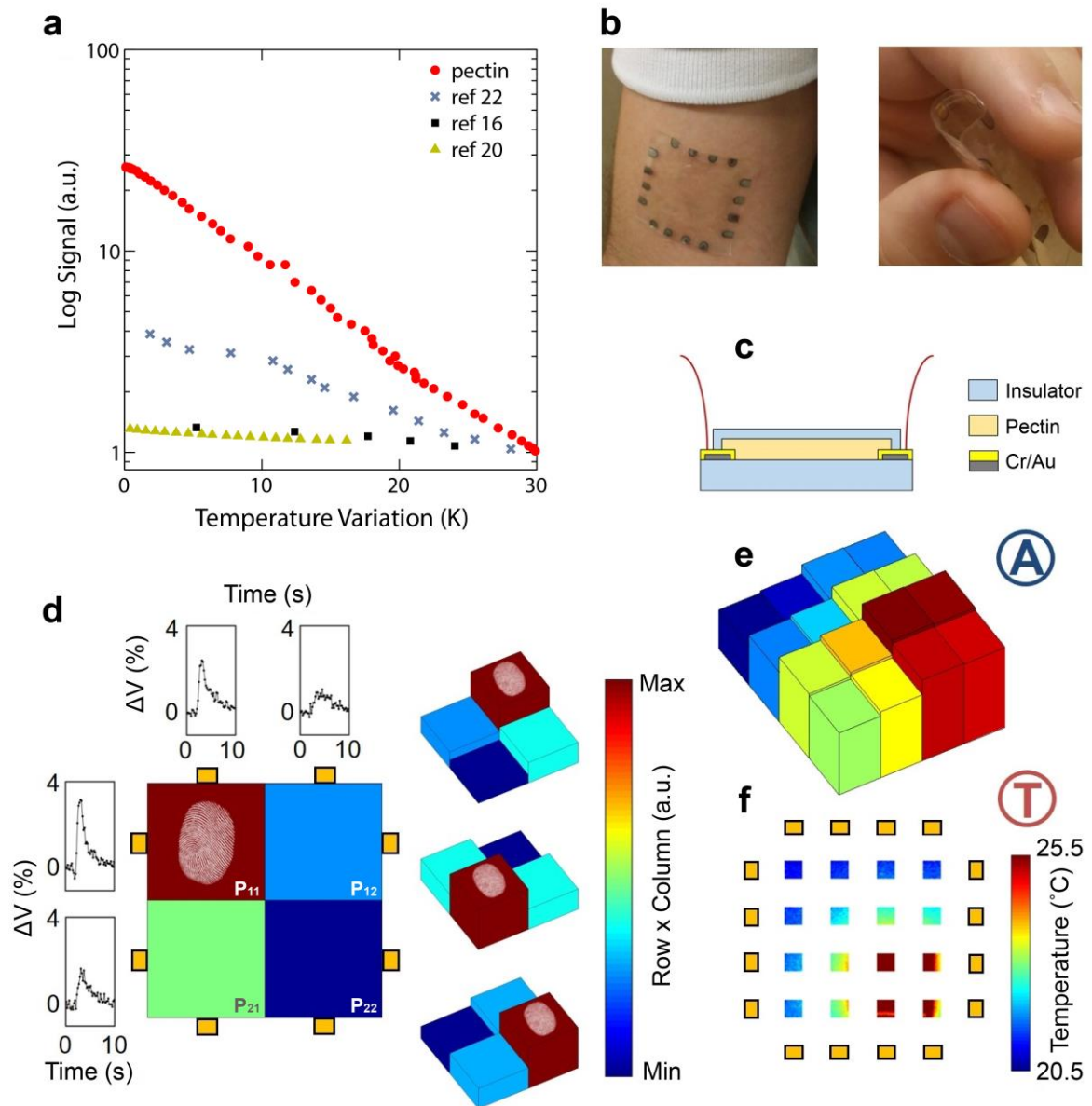


**Figure 3 | Characterization of the temperature sensing skins.** **a**, Responsivity of different synthetic skins. Normalized signal variation as a function of relative temperature change. Red dots: pectin film resistance. Blue crosses: resistance replotted from Park et al. Ref. 22. Black squares: voltage replotted from Kim et al. Ref. 16. Green triangles: resistance replotted from Segev-Bar et al. Ref. 20. **b**, Pictures of a 16-pixel skin with PDMS as bottom and top insulator. **c**, Schematic view of the pectin skins in cross section. **d**, Electrical response and temperature maps obtained with a 4-pixel skin, when a finger touched it in different positions (refer to the finger print location in each panel). The voltage-time panels show the signal readout for the corresponding rows and columns. The colors (and heights of the blocks) correspond to the product between the maximum signal variations (in %) detected in each row and column (see Supplementary Information, Tab. S1), normalized to 1. Figure S5 shows the percentage increase of the signal in time, for each of the 4-pixels when individually touched. **e**, Electrical response of a 16-pixel skin when a warm object is placed on its bottom right corner. **f**, Pixelated thermal camera image of the skin corresponding to (**e**).

# Supplementary Information

## Biomimicking pit vipers' infrared sensing

Raffaele Di Giacomo<sup>1</sup>, Luca Bonanomi<sup>1</sup>, Vincenzo Costanza<sup>1</sup>, Bruno Maresca<sup>2</sup> and Chiara Daraio<sup>1</sup>

<sup>1</sup>Department of Mechanical and Process Engineering (D-MAVT), Swiss Federal Institute of Technology (ETH), Zurich, CH, Switzerland.

<sup>2</sup>Department of Pharmacy, Division of Biomedicine, University of Salerno, Fisciano, Italy.

### Supplementary Material and Methods

The electrical measurements reported in Fig. 1c, 2d, 2e, S1, S2, S6, S8 were performed in a two-point contact geometry using a source measurement unit (Keithley model 2635), also referred to as amperometer or pico-amperometer in the main text of the paper. The electrical measurements in Fig. S10 were acquired with a lock-in amplifier model SR830 Stanford research systems. For the electrical measurements reported in Fig. 3 and S5, we applied sequentially a square wave voltage having an amplitude of 18V to the electrical contacts in each row and column. We measured the signal output with the readout circuit (in Supplementary Fig. S4), connected to a DAQ board (National Instruments® BNC-2110). The thermal camera used in the experiments is a FLIR® A655sc.

### Pectin

Pectin is composed of galacturonic acid for approximately 70% and all pectic polysaccharides contain galacturonic acid linked at the O-1 and the O-4 positions. Studies based on pectin biosynthesis have shown that pectin is synthesized in the Golgi apparatus and transported to the cell wall inside membrane vesicles<sup>1</sup>. Once synthesized polymers move to the cell wall by the movement of Golgi vesicles, possibly along actin filaments through their myosin motors<sup>1</sup>. The observed heterogeneity in the pectin structure is due to species-, cell type-, and developmental state-specific differences in enzyme composition<sup>2</sup>. Essentially, all studies on pectins have been performed on economically important plants such as apple, citrus, sugar beet, tomato or on cultured cells as sycamore, carrot, spinach, and rose. Thus, very little is known of the 235,000 remaining known flowering plants and of pectins of green algae, liverworts, mosses, and ferns. In addition, characterization of pectin from cell wall mutants<sup>3,4</sup> and from plants growing in extreme environments may reveal unknown pectin structures with different properties. Pectin biosynthesis probably requires at least 67 transferases (glycosyl-, methyl-, and acetyl-transferase). It includes homogalacturonan, rhamnogalacturonan I, and the substituted galacturonans rhamnogalacturonan II (RG-II), and xylogalacturonan (XGA)<sup>5</sup>.

In low-ester pectins, the gelation that occurs within the egg-box is due to the presence of calcium ions can be quickly reversed by monovalent sodium and potassium cations<sup>6</sup>. An initial dimerization step of two homo-galacturonic chains, by cooperative bridging through  $\text{Ca}^{2+}$  ions determines the binding of the first calcium cation to two pectin chains facilitating their alignment with respect to each other, allowing an easier binding of an upcoming calcium ion<sup>7</sup>.

## Pectin film

### Current-voltage characteristic

Figure S1 shows the typical current-voltage characteristic of a pectin film sample, as the one shown in Fig. 1a. The characteristic is linear, thus the device schematic in Fig. 1c represents a thermistor. The measurements were obtained with a source meter (Keithley model 2635).

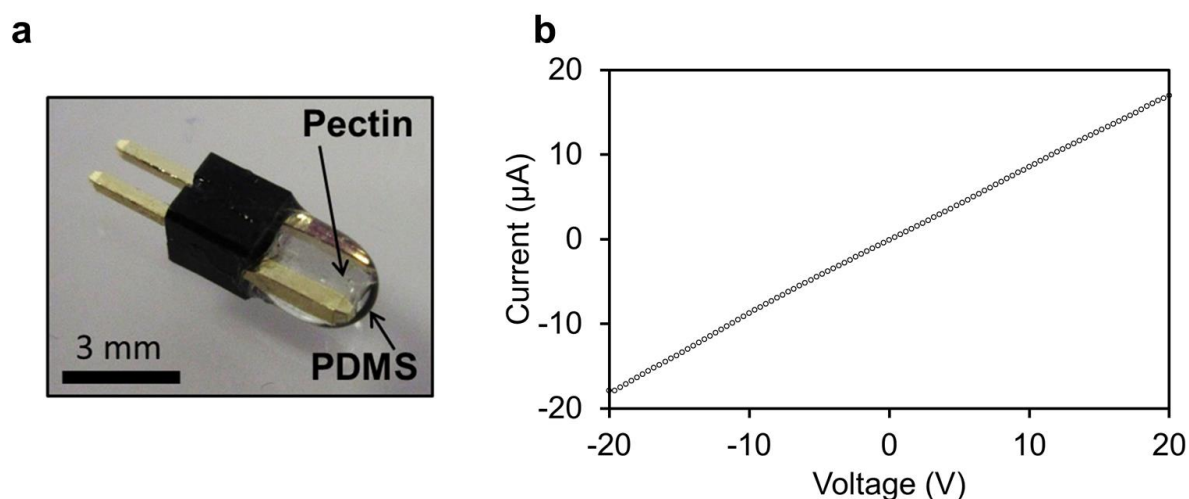


**Figure S1 | Pectin film thermistor.** **a**, Digital image of a small pectin film thermistor. **b**, Current vs. voltage characteristic of a pectin thermistor. Each circle represents a measurement point.

### Current-temperature characteristics

Figure S2a shows the temperature and current measurements as a function of time for the thermistor of Fig. 1a. The experiment was performed by increasing the temperature of the thermistor from 8 to 30 °C and then from 30 to 39 °C using a hotplate. The temperature was monitored using a thermal camera (FLIR a600) directly pointing to the thermistor, the setup is shown in Fig. 2a. The current across the device was monitored using a source meter (Keithley model 2635) and followed the temperature profile measured by the thermal camera. The temperature-current relation is exponential and it is shown in Fig. 1c, directly derived from Fig. S2.

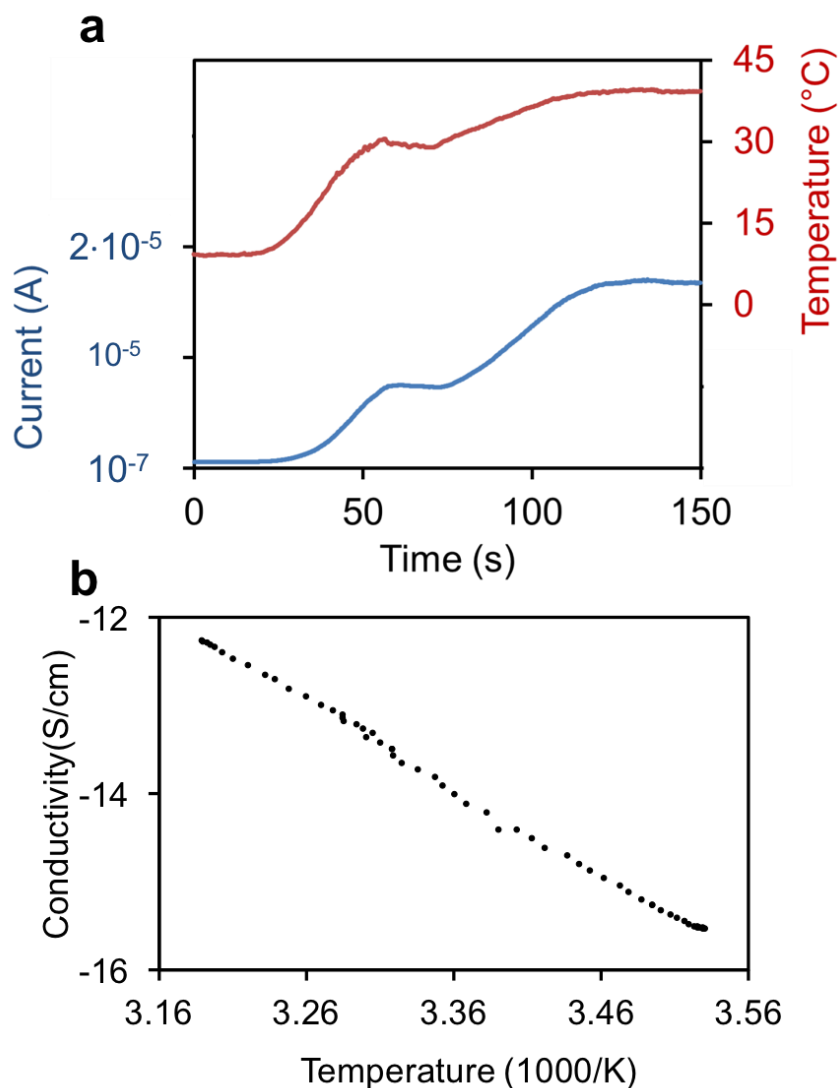


**Figure S2 | Current-temperature characteristics of the pectin thermistor in Fig. 1 and corresponding Arrhenius plot. a,** Temperature and current on a pectin thermistor as a function of time. The blue dots report the current measured in the thermistor. The red dots represent the temperature of the thermistor measured by the thermal camera. **b,** Arrhenius plot of electrical conductivity derived from Fig. S2a.

Figure S2b shows the Arrhenius plot of the conductivity of the pectin thermistor. The activation energy can be derived from the slope of the line in the Arrhenius plot, multiplying it by the gas constant, as follows:

$$E_a = \text{Slope} \times R = 9.85 \text{ K} \times 8.31 \text{ J K}^{-1} \text{ mol}^{-1} = 81.9 \text{ kJ mol}^{-1}$$

## Large area sensors

Supplementary Video 1 shows an experiment on a large area sensor performed with the setup in Fig. 2a. A cup of coffee (covering less than a ninth of the film's surface area) was placed in the middle of the film while electrical current was monitored as a function of time, in parallel to the acquisition by a thermal camera and an optical video. To explain the current measurements, we associated a lumped element model to the sensor area. The resistance of the uniform film is concentrated into nine resistors (3 branches of 3 resistors in series, as shown in the white schematic diagram superimposed to the digital images in the video) connecting the two electrodes (cyan lines in the video). We assumed that only the resistor under the cup is contributing to the current increase, in proportion to the area under the cup and to its temperature variation (see thermal images in the video). We also assumed that the resistance change under the cup corresponds to the measurements reported in Fig. 1a, from which we derived that  $R_{(30\text{ }^{\circ}\text{C})} = 0.36 \times R_{(22\text{ }^{\circ}\text{C})}$ . We measured a current change across the large area of  $\Delta I = 6.6\%$  between 22 and 30 °C. This value agrees with the assumption that the material has the same sensitivity as the one measured in the small film (Fig. 1a). The high responsivity of the pectin hydrogels is responsible for the ability to capture local events in large films, though without identifying the precise location and spatial dimension of the temperature source.

**Video S1 | Large area film testing.** Results of an experiment performed on a sample A4 paper size with carbon tape electrodes, supported by a glass substrate and covered with an acetate sheet. In the movie, at time frame,  $t = 1$  sec, we show on the left a flexible film sample, and on the right the same sample deposited on a glass slide for testing. At time  $t = 14$  sec, we show imaginary lines dividing the sensor in 9 areas and the corresponding lumped elements model composed of 3 parallel branches of 3 resistors in series. At time  $t = 19$  sec, we show that the resistor associated to the area heated by the cup changes color, to represent its dependence on temperature. At time  $t = 30$  sec, we show in parallel a thermal camera video (on the top left corner), the current measured across the sensor (in the top right corner), and the corresponding optical video with superimposed schematic of the electrical model (bottom left corner). At time  $t = 52$  sec we show the change in resistance estimated from Fig. 1a, which explains the change in current measured across the film, highlighted in cyan in the current-time plot.

## Temperature mapping skins.

Figure S3 shows the setup for the temperature measurement of films with multiple electrical contacts (herein referred to as “skins”). Figure S3a shows a 4-pixel configuration. The architecture of the skin is reported in Fig. 3c. The bottom insulator is made of silicon dioxide thermally grown on a silicon wafer, while the top insulator is a PDMS layer. Chromium/gold contacts were sputtered on the bottom insulator. The same configuration was used for the 16-pixel skin, shown in Fig. S3b.

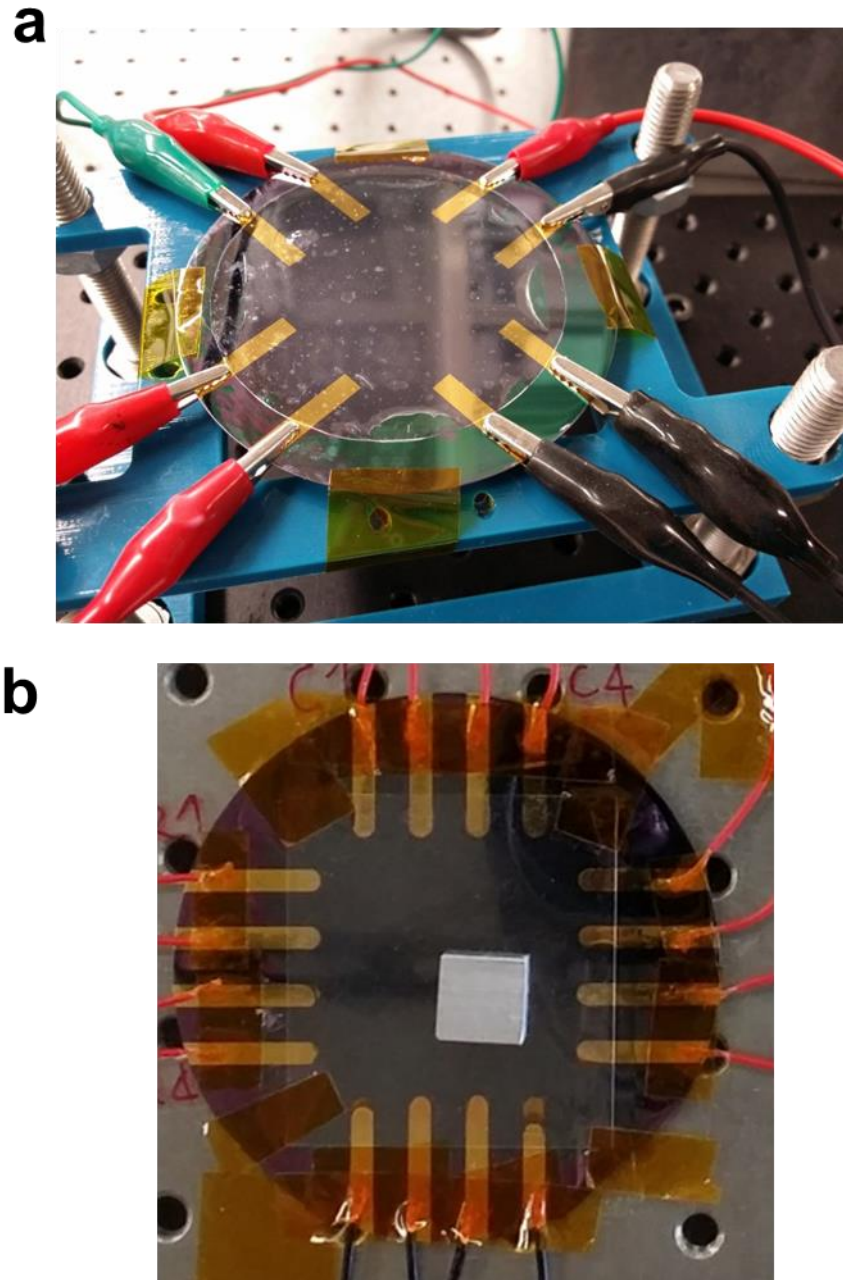


**Figure S3|Setup for the electrical measurements performed on skins. a, 4-pixel skin. b, 16-pixel skin.**

### **Read out circuit**

Figure S4 shows the schematic of the read out circuit used for the 4-pixels skin. Figure S4a shows a diagram of the working principle: when temperature increases in correspondence of the pixel P11, the electrical resistance decreases locally. Thanks to the high sensitivity, the variation of resistance affects the series of resistances of the entire row and column as in Fig. S4a. This principle is similar to the one showed in Supplementary Video 1. Thus the local change in resistance is conveniently measurable interrogating each row and column in a separate time interval. This is done by allowing current to circulate in the row or column by

switching on each CMOS couple. Only one row or column is on at any given time. Figure S4c shows an example of row 1 being read. Figure S4d shows the signals used to enable the reading. A buffer and an amplifier are used to condition and transfer the signals from the skin to the DAQ board. The DAQ read-out occurs when the enabling signal reaches its maximum value.

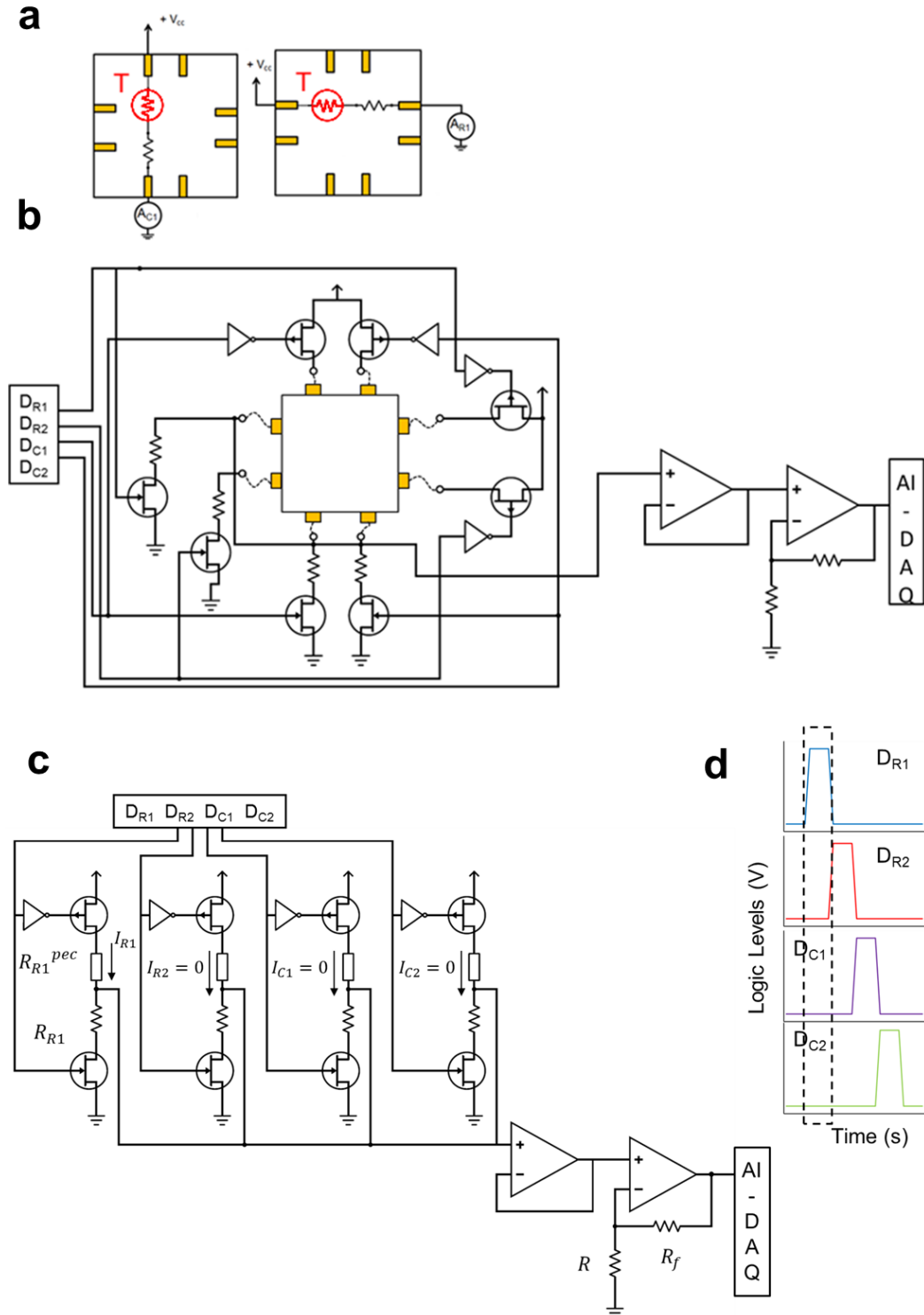


**Figure S4 | Read out circuit for the 4-pixel skin. a, Working principle. b, Skin connection. c, electrical schematic of the read out circuit when only one row is active. d, Enabling signals.**

### Measurement results on a 4-pixel temperature mapping skin

We report in Tab. S1 and Fig. S5 the results obtained from measurements on a 4-pixel temperature mapping skin. To obtain these measurements and locally increase the temperature on each pixel, we position a finger for  $\sim 2$  sec on a different quadrant of the skin. Table S1 shows the values representing the product of the signals in Fig. S5, when the finger is in each of the 4 positions (P<sub>11</sub>, P<sub>12</sub>, P<sub>21</sub>, P<sub>22</sub>). The table is obtained considering only the maximum voltage variation for each row and column (R<sub>1</sub>, R<sub>2</sub>, C<sub>1</sub>, C<sub>2</sub>). These values are multiplied as follows: R<sub>1</sub>C<sub>1</sub>, R<sub>1</sub>C<sub>2</sub>, R<sub>2</sub>C<sub>1</sub>, R<sub>2</sub>C<sub>2</sub>, the results are normalized for each experiment and reported in the schematics of Tab. S1. The sampling rate was 100 s<sup>-1</sup> and the averaging was 5 points per channel.

**Table S1 | Values corresponding to the block diagrams with color map shown in Fig. 3d.**

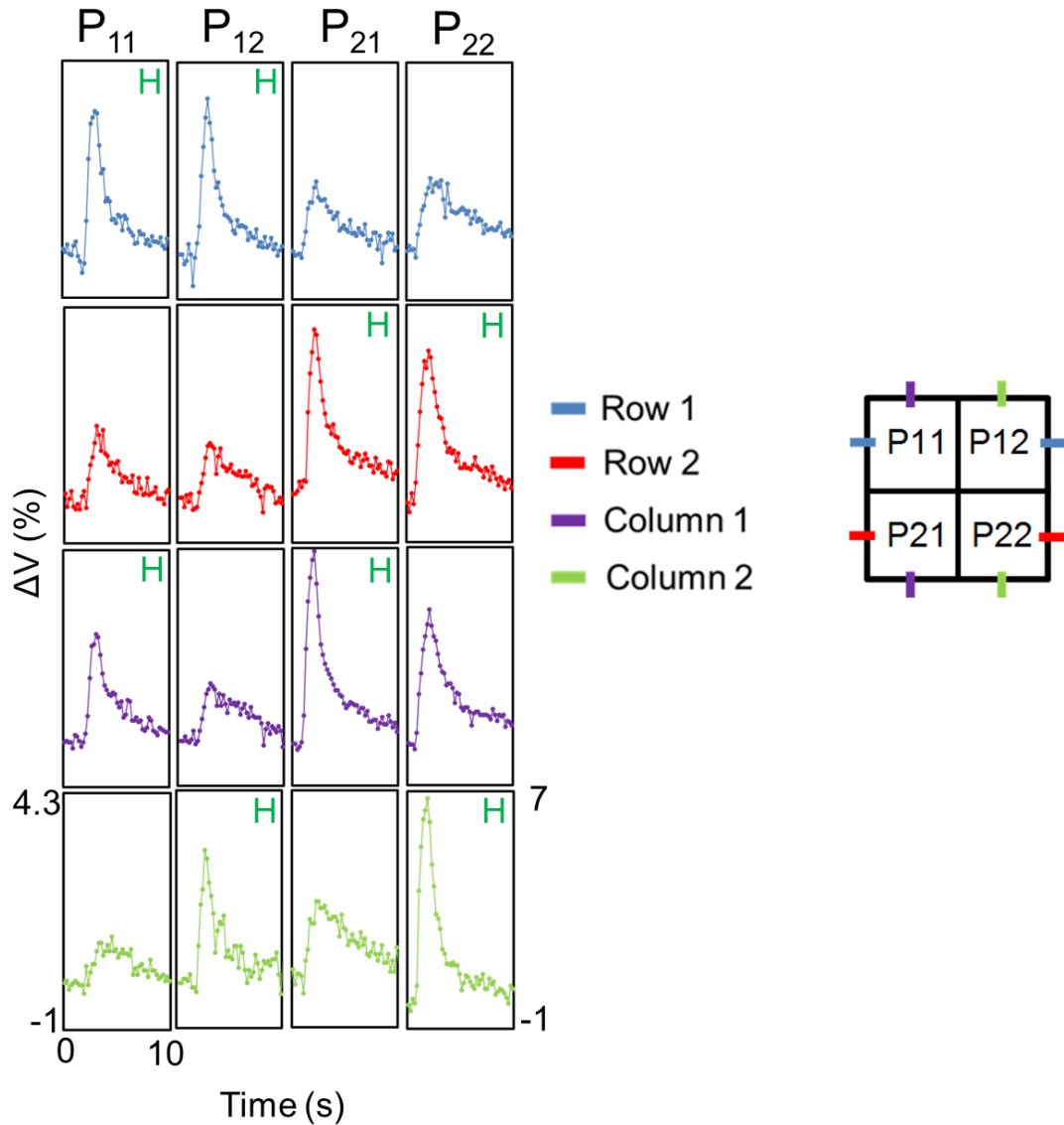
P11	C1	C2
R1	1	0.4
R2	0.6	0.2

P12	C1	C2
R1	0.4	1
R2	0.2	0.5

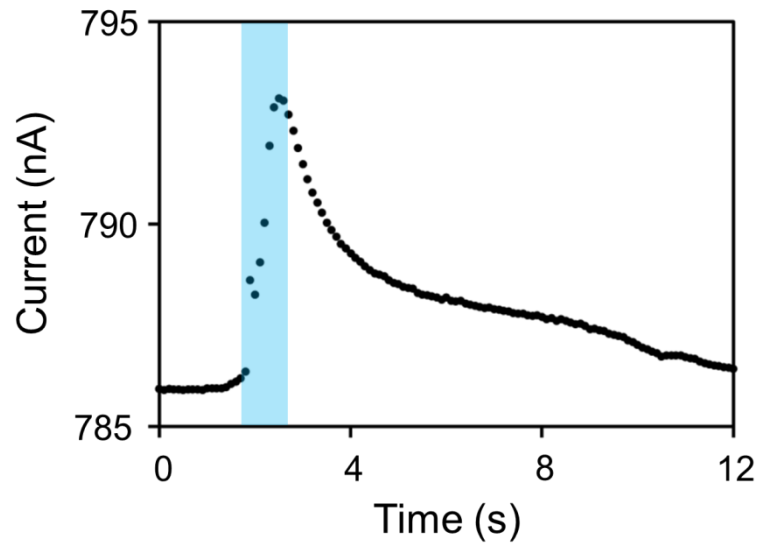
P21	C1	C2
R1	0.5	0.2
R2	1	0.5

P22	C1	C2
R1	0.3	0.5
R2	0.5	1



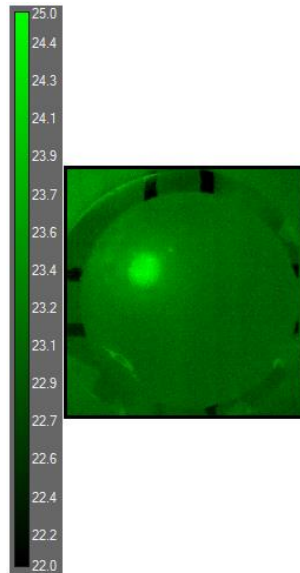
**Figure S5 | Voltage at the readout circuit for every row and column in a 4-pixel skin.** Light blue: signals from row 1. Red: signals from row 2. Violet: signals from column 1. Green: signals from column 2. All the time scales in the panels are between 0 and 10 sec. All amplitudes are between -1 and 4.3 except for P<sub>22</sub>, column 2, which is between -1 and 7 (as indicated in the corresponding panel). All signals for each finger position are acquired synchronously. The panels indicated by the letter “H” represent the highest signals for each row and column.

Figure S6 shows the current as a function of time in row 1 when P<sub>11</sub> is touched for ~1 sec. The noise level was undetectable, confirming that noise in the measurements of Fig. S5 was due to the readout circuit.



**Figure S6 | Current vs. time when the film is touched with a finger.** The black dots report the current measurements. The blue shadowed region represents the finger's contact time on the skin.

Figure S7 shows the thermal fingerprint on the film, as acquired by the thermal camera. The image was taken immediately after lifting the finger that was in touch with the skin for  $\sim 1$  sec. The temperature increase caused by the finger was less than 1 K, compared to temperature of the rest of the skin.



**Figure S7 | Thermal image of the skin just after being touched with a finger.** The image shows the temperature map obtained with the thermal camera after a finger touched the skin in position P<sub>11</sub> (light green area). All units in the color intensity bar are expressed in degrees °C.

To prove that the sensitivity of the skin is due to temperature changes and not pressure, we pressed the skin with a rounded metal part for ca. 5 sec, as shown in Fig. S8a (red panel). The

skin was then touched with a finger, for the same length of time (green panel). When the skin was in contact with the metal tip, which was approximately at the same temperature of the skin, its effect on the current-time plot was negligible. However, when the skin was in contact with the finger, which was warmer than the skin, a current increase was evident.

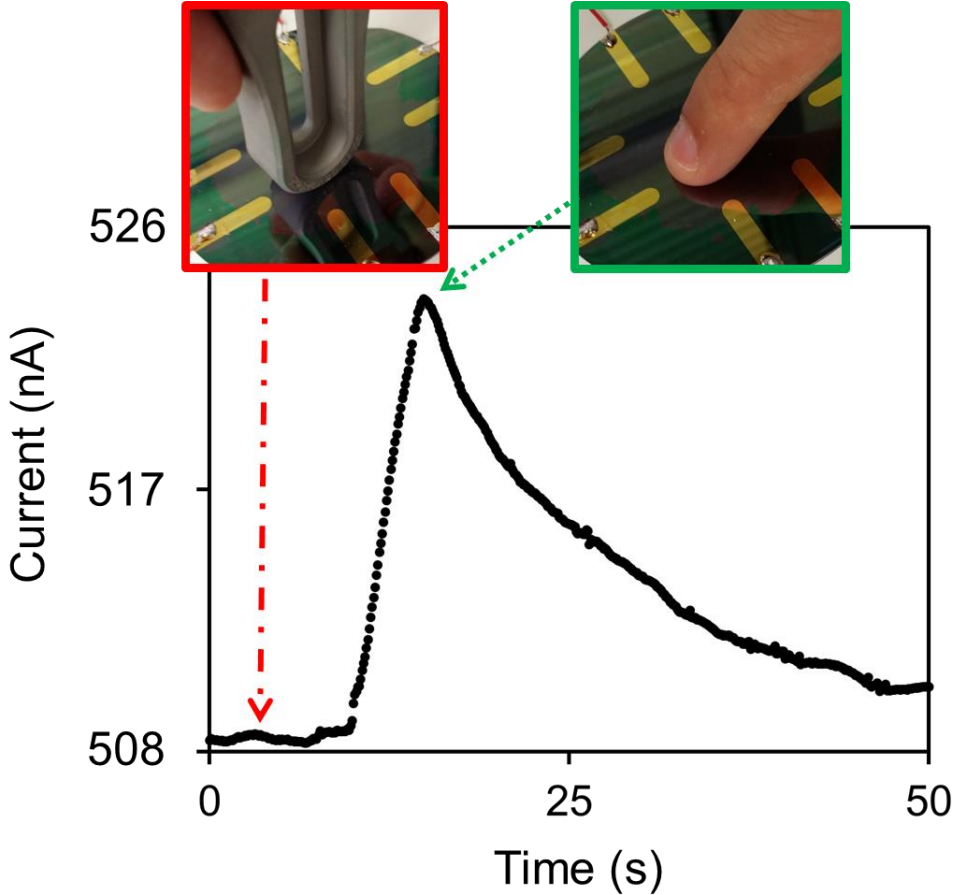


**Figure S8 | Effect of pressure and temperature on a 4-pixel skin.**

**Measurement results on a 16-pixel temperature mapping skin**

We tested a 16-pixel skin, as shown in Fig. S3b, placing a warm (26 °C) aluminum square in contact with the skin. Figure S9 shows the thermal image of the skin, obtained after 0.8 sec. This image corresponds to the pixelated picture in Fig. 3f. Table S2 shows the values obtained from the skin, reported in Fig. 3e. To obtain these values, the acquisition rate used was 10 samples/sec, which corresponds to 1.25 samples/sec/channel.

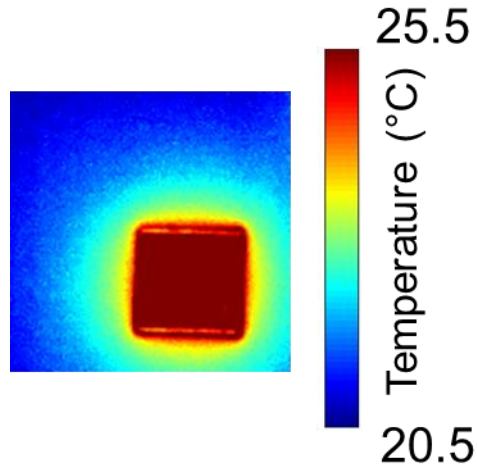


**Figure S9 | Aluminum square in contact with the 16-pixel skin.**

**Table S2 | Values corresponding to the block diagram with color map shown in Fig. 3e.**

	C1	C2	C3	C4
R1	0.45	0.49	0.59	0.59
R2	0.59	0.63	0.76	0.76
R3	0.77	0.82	1.00	0.99
R4	0.74	0.79	0.96	0.95

### Ac measurements

Figure S10 shows a typical thermal response measured at three different frequencies on the small pectin film samples shown in Fig. S1a. The current is reported in arbitrary units since it was measured as the RMS value of the voltage drop on a resistor (50 k $\Omega$ ) in series with the sample (see inset of Fig S10). No responsivity difference between measurements at different frequencies and d.c. measurements was found.

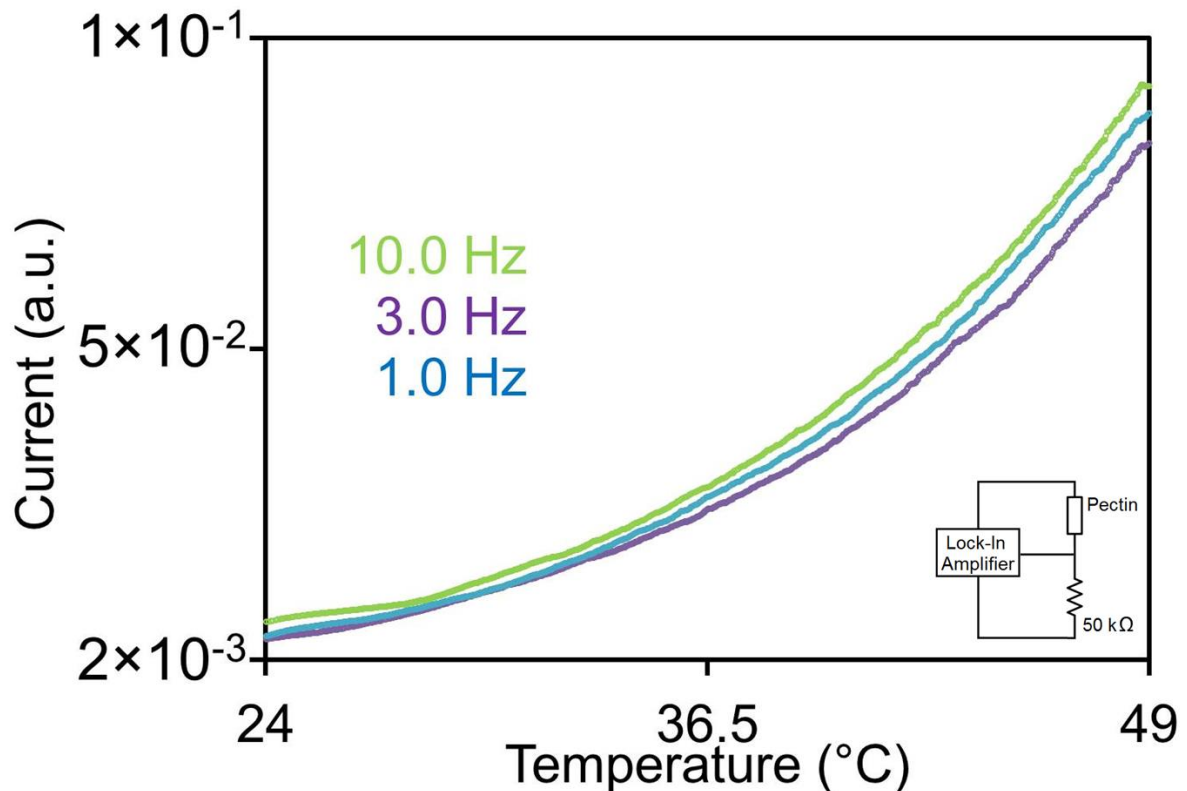


Figure S10 | Alternating current measurements on the pectin films.

## References

1. Nebenführ, A., Gallagher, L. A., Dunahay, T. G., Frohlick, J. A., Mazurkiewicz, A. M., Meehl, J. B. & Staehelin, L. A. Stop-and-go movements of plant Golgi stacks are mediated by the acto-myosin system. *Plant Physiol.* **121**, 1127-1142 (1999).
2. O'Neill, M. A., Ishii, T., Albersheim, P. & Darvill, A. G. Rhamnogalacturonan II: structure and function of a borate cross-linked cell wall pectic polysaccharide. *Annu. Rev. Plant. Biol.* **55**, 109-139 (2004).
3. Burget, E.G. & Reiter, W.-D. The mur4 mutant of arabidopsis is partially defective in the de novo synthesis of uridine diphospho L-arabinose. *Plant Physiol.* **121**, 383-389 (1999).
4. Reiter, W.-D., Chapple, C. & Somerville, C.R. Mutants of Arabidopsis thaliana with altered cell wall polysaccharide composition. *Plant J.* **12**, 335-345 (1997).
5. Mohnen, D. Pectin structure and biosynthesis. *Curr. Opin. Plant Biol.* **11**, 266-277 (2008).
6. Munarin, F. M., Tanzi, M. C. & Pertini P. P. Advances in biomedical applications of pectin gels. *Int. J. Biol. Macromol.* **51**, 681- 689 (2012).
7. Renard, C. M. G. C. & Jarvis M.C. Acetylation and methylation of homogalacturonans 1: optimization of the reaction and characterization of the products. *Carb. Poly.* **39**, 209-216 (1999).